Clim. Past Discuss., 6, 2071–2116, 2010
www.clim-past-discuss.net/6/2071/2010/
doi:10.5194/cpd-6-2071-2010

Climate of the Past Discussions

A regional climate simulation over the Iberian Peninsula for the last millennium

J. J. Gómez-Navarro[1], J. P. Montávez[1], S. Jerez[1], P. Jiménez-Guerrero[1], R. Lorente-Plazas[1], J. F. González-Rouco[2], and E. Zorita[3]

[1]Departamento de Física, Universidad de Murcia, Murcia, Spain
[2]Departamento de Astrofísica y CC. de la Atmósfera, Universidad Complutense de Madrid, Madrid, Spain
[3]GKSS Research Centre, Geesthacht, Germany

Received: 27 September 2010 – Accepted: 27 September 2010 – Published: 8 October 2010

Correspondence to: J. P. Montávez (montavez@um.es)

Published by Copernicus Publications on behalf of the European Geosciences Union.

Abstract

In this study we present a regional paleoclimate simulation which covers the last millennium over the Iberian Peninsula (IP) with an unprecedented resolution of 30 km. The simulation was performed with a climate version of the mesoscale model MM5 coupled to the global model ECHO-G. Both experiments were driven by the same reconstructions of several external factors. The high spatial resolution of the regional model allows to simulate realistically many aspects of the climate in the IP when comparing the simulation to an observational data set in a reference period (1961–1990). Although the regional model is strongly driven by the boundary conditions, it is able to develop a different realisation of the past climate, which has a strong impact in those exercises comparing the results of climate simulations versus proxy reconstructions. A preliminary comparison of the simulation results with reconstructions of temperature and precipitation over the IP allows to recognise several aspects where both approaches agree, as well as identify the disagreements and try to point out the possible causes.

1 Introduction

In the last years considerable efforts have been devoted to the understanding of the internal variability and its role in the evolution of the climate in the last millennia (Bradley and Jonest, 1993; Jones et al., 2001; Zorita et al., 2005; Mann et al., 2008; Swingedouw et al., 2010, among others). This has allowed to frame the short instrumental period in a broader climatic context, and to understand some the of physical mechanism responsible for the observed variability.

These efforts belong to two categories: climate reconstructions based on proxy indicators and climate model simulations. The former uses information from various indirect sources, including documentary records, tree rings, ice cores, etc. These sources provide information at different temporal resolution about the past evolution

CPD
6, 2071–2116, 2010

of temperature and precipitation, among other variables (Bradley and Jonest, 1993; Jones et al., 2001; Luterbacher et al., 2004; Mann et al., 2008). On the other hand, the use of comprehensive atmosphere ocean global circulation models (AOGCM) has become possible due the impressive increase in computational power. This has allowed to perform simulations with state-of-the art global climate models over periods of several centuries (Zorita et al., 2005; Tett et al., 2007; Ammann et al., 2007; Swingedouw et al., 2010). Although the validation of these comprehensive models used for future climate projections can be performed by checking whether they are able to reproduce the main features of the actual climate, for instance whether or not they simulate a present climate consistent with the observations, the reliability of climate models to realistically simulate climate changes is much more difficult to asses. The comparison of simulations of past climates with climate models against proxy-based climate reconstructions may thus increase the confidence put on future projections or identify drawbacks that should be corrected, thus improving the climate projections as well (Gonzalez-Rouco et al., 2009).

However this comparison is burdened by two important factors. On the one hand climate reconstructions are based on data that is usually local or regional, whereas the present AOGCMs have a too coarse spatial resolution which precludes a realistic representation of the local features that may strongly influence proxy records. This may cause important mismatches between simulations and reconstructions. So far, the comparison between model simulations and climate reconstructions over the past millennium has been limited to global or hemispheric scales (Jones et al., 2009). Several authors have also used a number of methodologies trying to overcome this problem. Stevens et al. (2008) grouped borehole temperature profiles into regional ensembles, to make their local information compatible with the spatial scales of the AOGCM ECHO-G, which implements a spatial of about 3.75°. These authors have, however, underlined the need for finer spatial resolution simulations. On the other hand the climate system fluctuates internally over a large frequency range, from days to million of years (Huybers and Curry, 2006). Climate models are also affected by this

CPD
6, 2071–2116, 2010

natural random variability, and hence one should not expect a complete agreement at interannual timescales when comparing the temporal evolution of model simulations and reconstructions, even if both are perfect (Yoshimore et al., 2005).

Regarding the scale gap between model and reconstructions, downscaling techniques are a common tool for meteorological and climate studies. Driven by a AOGCM simulation, these techniques allow to take into account the effect of regional features, thus developing a more realistic climate for a limited area. In particular, dynamical downscaling methods, involving the use of Regional Circulation Models (RCM), solve similar equations a AOGCM does, but using higher resolution for a limited area domain. The higher spatial resolution, which implements a more realistic orography, and improved physical parametrisation of RCMs allow them to simulate the features of regional climates more accurately than current AOGCMs, and for this reason RCMs are extensively employed in climate change projections within the context of large projects such as PRUDENCE or ENSEMBLES (Jacob et al., 2007, and references herein). Nevertheless, to date there are few studies where these models have been used for paleoclimate applications (Zorita et al., 2010), or mostly focusing in periods farther back in the past (Hostetler et al., 2000).

In this the study, we present the first results of a simulation performed with the regional model MM5 driven by the global model ECHO-G over the last millennium (1001–1990) for a domain encompassing the Iberian Peninsula (IP). This area presents sharp spatial contrasts of temperature and precipitation due to its complex topography and its location at the southern fringe of the North Atlantic storm tracks. Hence it provides a good test bed to examine the skill of regional models in a paleoclimate context. For example, the precipitation in the south-western part of the IP is strongly influenced by the North Atlantic Oscillation (NAO), whereas precipitation in the northern fringes and the regions located along the Mediterranean coasts is much more weakly connected to the North Atlantic weather systems.

To date, there are nevertheless few climate reconstructions for this region to compare against the simulations. For this study we use the gridded reconstructions of

CPD
6, 2071–2116, 2010

monthly, or seasonal, temperature and precipitation for the Western European region (Luterbacher et al., 2004; Pauling et al., 2006).

The paper is organised as follows: in Sect. 2 we describe the experiment set up of both the AOGCM and the RCM, as well as the proxy reconstructions used for comparison with the simulations. We also describe some of the analysis tools employed in the paper. In Sect. 3 we evaluate the added value provided by MM5 to the climatology developed by ECHO-G for a reference period. For this purpose we use a simulation driven by meteorological reanalysis. In Sect. 4 we summarise the main features of the whole simulation, focusing on the differences between both models, and also compare the simulation with several proxy-based reconstructions for the area of study. Discussions and conclusions are given in Sect. 5.

2 Description of simulations, data employed and methodology

For this study we have performed two simulations using different sets of driving conditions for a climate version of the regional model MM5. The first experiment (hereafter referred to as ERA40 + MM5) is driven by ERA40 reanalysis (Uppala et al., 2005) for the period 1961–1990. Jerez et al. (2010) have already shown that this simulation is capable of reproducing realistically the main features of the climate in the IP, in particular considering temperature. The second experiment (hereafter referred to as ECHO-G + MM5) has been driven by the global model ECHO-G, and covers the last millennium almost entirely (1001–1990). We use the climate simulated in the first experiment, together with an observational data base, to benchmark the skill of the regional model to reproduce the present climate when it is conducted by ECHO-G.

The ECHO-G global model driving the long RCM paleosimulation consists of the spectral atmospheric model ECHAM4 coupled to the ocean model HOPE-G (Legutke and Voss, 1999). The model ECHAM4 was used with a horizontal resolution T30 (~3.75° × 3.75°) and 19 vertical levels. The horizontal resolution of the ocean model is approximately 2.8° × 2.8°, with a grid refinement in the tropical regions and 20 vertical

CPD
6, 2071–2116, 2010

levels. A flux adjustment constant in time and with zero spatial average was applied to avoid climate drift. The model was driven by estimations of three independent sources of external forcings: greenhouse gases (GHGs) concentrations in the atmosphere, total solar irradiance (TSI) and an estimation of the global radiative forcing of stratospheric volcanic aerosols. The last two effects are included through the introduction of variations in an effective solar constant. A full description of this simulation and their external forcings can be found in Zorita et al. (2005) and references herein.

The evolution of these forcings is depicted in the Fig. 1. The orange line represents the reconstruction employed for the variability of the TSI. Black lines show the estimated reduction in solar irradiance at the top of the atmosphere caused by volcanic eruptions. The sum of both lines is the effective solar constant, which is implemented in the model to take into account both sources of external forcing. There is a series of maxima and minima in the TSI of which three minima around 1440, 1700 and 1810 stand out. These minima drive three respective minima in the global near surface-air temperature (SAT) (see Fig. 10), which match known cold periods in the past, as further explained below. Finally, green, blue and grey lines represent the evolution of nitrogen dioxide, carbon dioxide and methane, respectively. GHGs concentrations show a relatively constant value until 1850, roughly when the industrial period begins. Since then, both GHGs concentrations increase globally until the end of the simulated period in 1990. The models, AOGCM and RCM, have been driven by identical external forcings to avoid physical inconsistencies.

The regional climate model used for the present study is a climate version of the fifth-generation Pennsylvania-State University-National Center for Atmospheric Research Mesoscale Model (Dudhia, 1993; Grell et al., 1994; Montávez et al., 2006; Gómez-Navarro et al., 2010). Figure 2 depicts the spatial resolution implemented in the AOGCM (up) together with the two two-way nested domains with a resolution of 90 km and 30 km respectively employed in the RCM simulation (down). The outer domain (D1) covers Europe and the Mediterranean Sea since this area strongly influences the climate of the eastern part of the Iberian Peninsula (Font-Tullot, 2000). The inner

CPD
6, 2071–2116, 2010

domain (D2) covers the IP with higher resolution. The atmosphere is represented by 24 sigma levels in the vertical, with the top level at 100 hPa. The boundary conditions of the model ECHO-G are introduced into the outer domain of the RCM through a blending area of five grid points at the fringes of the outer domain, shown in grey squares in Fig. 2. This area is excluded from the analysis hereafter.

The physics configuration in the RCM has been chosen in order to minimise the computational cost, since none of the tested configurations provides the best performance for all kinds of synoptic events and regions (Fernandez et al., 2007). The physical options implemented here are: Grell cumulus parametrisation (Grell, 1993), Simple Ice for microphysics (Dudhia, 1989), RRTM radiation scheme (Mlawer et al., 1997) and MRF for boundary layer (Hong and Pan, 1996). The Noah Land-Surface model (Chen and Dudhia, 2001a,b) has been used, as it simulates more accurately the climate in dry areas, specially in summer over most of the IP (Jerez et al., 2010). Boundary conditions for D1 are updated every 6 h in the ERA40 + MM5 experiment, and every 12 h in the ECHO-G + MM5 simulation.

In order to illustrate the added value provided by the model MM5, we compare the seasonal mean values of SAT and precipitation in a reference period (1961–1990) in the four data sets (ECHO-G, ERA40, ECHO-G + MM5 and ERA40 + MM5) with the European Climate Assessment and Observations database (ECA) (Haylock et al., 2008). The ECA data set is a reconstruction of the evolution of SAT and precipitation for the recent past (1950–2006). It is the result of an interpolation of observational data to a high resolution regular grid that homogeneously covers Europe over land grid points. This data set is commonly used for model validation purposes in large projects such as ENSEMBLES (Jacob et al., 2007).

This comparison has been performed by means of Taylor diagrams (Taylor, 2001). These depict, in a polar coordinates graph, the correlation and variability ratio of two series. However, instead of showing correlation and variability of two temporal series, as the usual approach, the Taylor diagrams we show here represent the spatial correlation and standard deviation ratio of two gridded spatial fields. To make all data sets

CPD
6, 2071–2116, 2010

comparable, the data of the four simulations have been spatially interpolated to the ECA grid, which is a 0.25° × 0.25° regular grid, resulting in a total of 1209 grid cells over the IP after removing the ocean grids.

In order to further evaluate similarities between the ECHO-G + MM5 and ERA40 + MM5 simulations, we have performed an Empirical Orthogonal Function (EOF) analysis to the seasonal series of SAT and precipitation. This methodology reduces the high dimensionality of these fields decomposing them into spatial patterns (EOFs) and associated principal components (PCs) (von Storch and Zwiers, 2007). By comparing the EOFs of both simulations we can get some insight about the differences and similarities of their spatial correlation structure.

Finally, some preliminary comparisons against proxy-based climatic reconstructions have been performed. We have employed the SAT reconstruction by Luterbacher et al. (2004) and the precipitation reconstruction by Pauling et al. (2006). Both data sets consist on monthly and seasonal series in a 0.5° × 0.5° regular grid over Europe. They are based on a large variety of long instrumental series, indices based on historical documentary evidence and natural proxies. These reconstructions have been performed with a Climate Field Reconstruction method. The reconstruction method is based on principal components (PC) regression, by which a multivariate statistical regression model is set up between the leading Principal Components of a gridded observational data set and the available proxy records. This statistical model is then used to reconstruct the temperature or precipitation Principal Components backwards in time and, by combining the reconstructed PCs with the spatial eigenvectors, the whole spatial field.

3 Added value by the RCM

This section aims to show the added value by the RCM with respect to the AOGCM simulation. We compare the climatologies generated by MM5 when this regional model is driven by ECHO-G and ERA40 in a 30-yr reference period (1961–1990). Jerez et al.

CPD
6, 2071–2116, 2010

(2010) illustrated how the downscaling of ERA40 performed with MM5 is capable to reproduce the main features of the SAT of the IP, but no equivalent study has been performed for precipitation so far. For this reason we have also compared the results of the simulations with the ECA data base, which contains information about SAT and precipitation and it is commonly used for validation purposes.

3.1 Mean values

Figure 3 shows the mean value of the seasonal SAT for the reference period for all data sets. Each column depicts the result for each of the four models and the observational data set in this order: ECHO-G, ERA40, ECHO-G + MM5, ERA40 + MM5 and ECA. Each row represents the mean climatology broken down by season. The large difference between ECHO-G and ERA40 (first and second columns, respectively) in noticeable. This difference is attributable to their different spatial resolution (coarser in ECHO-G), but also to the fact that the reanalysis data incorporates the information from observations of the actual climate (Uppala et al., 2005). For this reason, ERA40 can be considered, in general, a more reliable realisation of the recent past. Comparing both data sets, ECHO-G tends to develop too cold summers and too warm winters, leading to an underestimation of the amplitude of the annual cycle. Furthermore the spatial resolution of ECHO-G does not permit to capture the orography of the IP (see Fig. 2a). In particular, the model is not capable of representing realistically some characteristic of the south of the IP, since it is defined as ocean grid-cells.

On the other hand, columns 3 and 4 in Fig. 2 show the result of nesting MM5 into the former data sets. The similarities between these simulations are noticeable, and are also similar to the observations depicted in column 5. The resolution of MM5 is able to take into account the main geographical characteristics of the IP, as can be noticed by the cold areas in both columns, which correspond quite well with the higher altitude regions (see Fig. 2b). Important differences still remain, such as an underestimation of the SAT in the southwestern parts of the IP in summer, and an overestimation of winter SAT in the central region. This underestimation of the amplitude of the annual cycle

CPD
6, 2071–2116, 2010

seems to be predetermined by the driving AOGCM. Hence, although MM5 ameliorates this deficiency, it is not able to correct it completely.

A similar picture is found for precipitation (Fig. 4). ECHO-G and ERA40 develop different rainfall patterns (see columns 1 and 2). In general, ECHO-G underestimates the amount of precipitation, more notably in the wettest parts of the IP in the North. This underestimation is stronger in winter and spring. The differences may be due to the coarser resolution of ECHO-G, which fails to discriminate between land and sea points at regional scale, but also to differences in the local and global circulation, as further commented below. As in the case of SAT, MM5 tends to narrow these differences, as can be appreciated in columns 3 and 4. In the case of precipitation there are nevertheless larger differences between the regional simulations. The main one is the overestimation of the precipitation in the Northwest of the IP in winter and autumn. Precipitation is underestimated in the south in warmer seasons.

An important aspect to take into account in the former comparisons is the fact the the ECHO-G model does not include assimilation of observations. Due to the internal random variability of the AOGCM, some of the main circulation modes in the model may not be simultaneous with those observed in the actual climate. In the ERA40 reanalysis this temporal evolution should in theory match the observed one, since it does include observational data assimilation. Thus, some of the differences in the ECHO-G + MM5 and ERA40 + MM5 simulations in the 30-yr period we have used as reference could be attributable directly to this cause, which is independent of the skill of the regional model. In particular, the precipitation in the IP is known to be strongly influenced by the NAO (Trigo et al., 2004), so differences in the state of this circulation mode in the reference period may explain part of the bias in the amounts of precipitation.

The improvement achieved by MM5 can be visualised in the Taylor diagrams (Fig. 5). In these diagrams we compare, by season, the performance of the four models when reproducing the mean SAT and precipitation in the reference period compared to the ECA data base. In particular each triangle in the figure depicts in polar coordinates the spatial correlation (angle) and standard deviation ratio (radius) between SAT mean

CPD
6, 2071–2116, 2010

values of each experiment and ECA. Similarly, each diamond represents the same calculation for precipitation. Climatologies of the four experiments have been previously interpolated to the ECA grid to perform the calculations. ECHO-G underestimates SAT spatial variability in all seasons, as expected due to its coarse resolution. ERA40 performs better in this respect, although it is still not able to represent the many variations in the climate over the IP. When the RCM is driven by both data sets, it simulates a very similar variability, which is also close to the observed. Although this may be partly due to the similar spatial resolution of both, the RCM simulations and the ECA data base, it is evident that the use of MM5 improves the simulations. Regarding the correlation, MM5 simulates a SAT pattern in both experiments which correlates by 0.95 with the observed one for each season, further highlighting the added value of the regional model. For precipitation we find a more complex behaviour. As before, ECHO-G systematically underestimates the spatial variability due the its coarse resolution. The correlation with the observations is high in summer because it is able to reproduce the observed north-south pattern, but in other seasons it is very low. MM5 is able to improve both aspects, and the correlation between precipitation with observations is over 0.8 for all seasons. Correlation between precipitation in ERA40 and ECA is high in general, and thus MM5 is not able to improve this aspect very much. ERA40 + MM5 shows, in general, lower spatial variability than ERA40, in some cases narrowing the differences between model and observations and in some others increasing them.

Summarising Figs. 3 to 5, MM5 is able to improve several aspects of the present climate simulated by ECHO-G. On one hand, it increases the amplitude of the SAT annual cycle, which is underestimated by the AOGCM. The seasonal mean values of precipitation and SAT are strongly modulated due to the higher spatial resolution. The RCM narrows the differences between the climatological values of SAT and precipitation in ECHO-G and ERA40, which become very similar to the observations, as indicated by the Taylor diagrams. This points to a better characterisation of the climate over the IP in the reference period when the outputs of ECHO-G are used to drive MM5.

CPD
6, 2071–2116, 2010

As indicated above, the main drawbacks in the climatologies of the ECHO-G + MM5 simulation with respect to ERA40 + MM5 are the underestimation of the amplitude of annual cycle of temperature and the overestimation of the winter precipitation in the northwest. Besides the problems with the internal variability of the AOGCM in the reference period commented above, both biases could be explained by an overestimation of the zonal circulation in the atmospheric model ECHAM4, a feature common in many global climate models. In winter, the extra warm and wet oceanic wind is conductive of warmer temperatures to the IP, whereas in summer it tends to cold it. This explanation is supported by Demuzere et al. (2009), who have shown that the model ECHAM5, the follow-up model version of ECHAM4 used in the present work, tends to develop a zonal circulation stronger than observed.

3.2 Variability

We have also examined the effect of MM5 on the simulated variability of SAT and precipitation. The standard deviations of the seasonal mean series of SAT are shown in Fig. 6. As in Figs. 3 and 4, columns 1 and 2 show the results for ECHO-G and ERA40. The main difference between these patterns is the strong underestimation of the variability in winter and autumn in ECHO-G. Nevertheless, the underestimation is not constant through the four seasons, and in fact the variability in some areas of the north of the IP in summer and spring is overestimated with respect to ERA40. The corresponding simulations when MM5 is coupled to both data sets are shown in columns 3 and 4 of the same figure, and column 5 depicts the same data for the ECA data base. ECHO-G + MM5 systematically underestimates the SAT variability with respect to ERA40 + MM5, and there are large differences in their spatial structure, the mismatch being more noticeable in spring. Nevertheless the RCM is able to correct some of the main deficiencies of ECHO-G. For instance, it increases the variability in autumn and winter, and decreases it in the North in summer, making the structure of the SAT variability more similar to the observations. Thus, the effect of MM5 is to

CPD
6, 2071–2116, 2010

correct ECHO-G by increasing and decreasing variability, depending on the season and area, but in all cases narrowing differences between ECHO-G and ERA40, and reducing differences with respect to ECA.

Figure 7 depicts the same information regarding the variability of the seasonal mean precipitation. As it could be expected, the wettest areas show a larger variability in every experiment. It is apparent that ECHO-G strongly underestimates the precipitation variability in all seasons, more noticeably in summer (see columns 1 and 2). MM5 corrects some of these differences, increasing the variability in many areas. In particular, the pattern of precipitation variability is very similar in ECHO-G + MM5 and ERA40 + MM5 (see columns 3 and 4), although there exists some underestimation of the precipitation variability in the Northwest of the IP in the ECHOG + MM5 experiment, mainly in the wettest areas. This contrasts with the fact that this simulation develops stronger precipitation amounts than ERA40 + MM5 (Fig. 4). These larger precipitations, together with their less variability, may be attributable to deficiencies in ECHO-G in reproducing the weather types that affect the climate over the IP, as well as a differences due to internal variability.

Summarising, ECHO-G tends to underestimate the regional variability of SAT and precipitation over the IP in the reference period respect to ERA40. MM5 is able to correct this drawback, with a general increase of variability. Furthermore it also corrects the overestimation of SAT variability in the North of the IP in summer. The improvements introduced by the downscaling process may have an important impact in inter comparison exercises between proxy reconstruction and simulations, since the former are strongly influenced by local climate features, which are better reproduced by the RCM. For instance, there are areas with great potential for proxy studies, such as the Pyrenees, and other mountain ranges in the southeast of the peninsula, in which MM5 clearly outperforms ECHO-G. Hence, comparison studies between ECHO-G + MM5 and reconstructions offer better reliability than between those and the AOGCM alone.

CPD
6, 2071–2116, 2010

3.3 Main variability modes

Finally, we have investigated the coherence of the covariance structure in the regional experiments driven by ECHO-G and ERA40 by means of an Empirical Orthogonal Function (EOF) analysis. This technique has been applied to the seasonal series of SAT and precipitation in the period 1961–1990 only over land grid points. It is important to note that the spatial patterns in the figures below are dimensionless, as they have been normalised to unit spatial variance. Hence, comparing the patterns does not indicate the amplitude of variability in each experiment, but only the relative spatial distribution of the correlation among the grid-cells. The comparison of the actual variability of both simulations has been presented in Figs. 6 and 7.

Figure 8 depicts the first three EOF patterns of SAT. The order of the maps is as follows: columns 1 and 2 show the first EOF for ECHO-G + MM5 and ERA40 + MM5, respectively. The second EOF for ECHO-G + MM5 and ERA40 + MM5 are shown in columns 3 and 4. Finally, the third EOF is shown in columns 5 and 6. Different rows represent the values per seasons, going from spring (first row) to winter (last row). The percentage of variance explained by each EOF is shown in Table 1. In both experiments and all seasons the percentage of variance explained by the first EOF is higher than 75%. The associated patterns present the same sign over the IP, and their shape is similar in both simulations. In summer, the form of the patterns seems to be related to the distance to the ocean, whereas in autumn they are rather correlated to altitude. It is interesting to note that a similar annual cycle in the variability patterns has been found in an ensemble of climate change projections (Gómez-Navarro et al., 2010). There are nevertheless important differences between simulations. In winter ECHO-G + MM5 develops a north-south pattern which does not match the west-east pattern found in ERA40 + MM5 very well. The second and third EOFs explain much less percentage of variance in all cases, with similar amounts in both simulations. This supports the similarities between both simulations. The overall form of these patterns is in this case very similar. The largest differences are found in the third EOF patterns for

CPD
6, 2071–2116, 2010

winter, although the percentage of variance explained by these patterns is only around 3%.

Figure 9 depicts the EOF patterns for precipitation. Table 2 shows the percentage of variance explained by each pattern. The percentage of variance explained by first EOF is in this case lower. An apparent exception occurs in winter, for which the EOF explains a high percentage of variance, coherently in both experiments. Regarding the spatial structure of the leading EOF, it is pretty similar in both simulations, being more marked in the wettest areas, which are the north-west in coldest seasons and the higher altitude areas in the north-east of the IP in summer. There are nevertheless important differences in spring, and in autumn. ECHO-G + MM5 tends to overestimate the intensity of the EOF pattern in the north-west, developing a pattern similar to that for winter. This difference could be explained again by the overestimation of the zonal circulation in ECHO-G. This stronger flow of humid air forces the RCM to simulate precipitation events in autumn that are not present when the RCM is driven by ERA40. This may point to an unrealistic frequency of certain weather types in the ECHO-G simulation, which leads to a misrepresentation of the precipitation variability in ECHO-G + MM5 in the warmer seasons, and can also affect the SAT field. The second and third EOF are more relevant in this case, as they explain an important percentage of variance. Their patterns are shown in columns 3 to 6. There exists overall a good agreement between the two simulations. The largest differences occur in summer, as ERA40 + MM5 tends to develop a more pronounced pattern in the high-altitude areas, as corresponds to a system weakly forced by advective flow. It is interesting to note that in autumn the ordering of the second and third EOF seem to be swapped in both experiments. This is not surprising since the percentage of variance explained by these two EOFs for ERA40 + MM5 is pretty similar, 13.42 and 13.30, respectively (see Table 2).

Overall, there is a relative good agreement between the EOF patterns in both experiments. In particular the EOF patterns varies coherently through the seasons and along the EOF hierarchy. The SAT patterns obey to an annual cycle similar to the one

CPD
6, 2071–2116, 2010

found previously in an ensemble of climate change projections (Gómez-Navarro et al., 2010). Regarding precipitation, there is a good agreement in winter, although several differences appear in summer, linked to the overestimation of the zonal flow. Hence, not only mean values and variability are similar between the climatologies developed by MM5 when coupled to ECHO-G and ERA40, but also the main variability modes are quite similar (with some deficiencies). This supports the idea that the dynamic downscaling of ECHO-G simulation is able to capture the main features of the present climate of the IP. Thus, it can be expected that the RCM will also be able to reproduce the actual features of past climates. It is important to highlight that the dynamic downscaling process is able to display spatial gradients at regional scale that the AOGCM can not. For instance, precipitation in the Northwest of the IP is dominated by the zonal flow from the Atlantic Ocean, whereas its effect in the south-eastern areas is weaker. These details, which are due to regional features and are implicitly included in the proxy reconstructions, can barely be simulated by a coarse resolution AOGCM.

4 Climate in the last 1000 yr in the IP

In the former section we evaluated the added value of the RCM simulation and illustrated how the dynamic downscaling process is able to narrow the differences between ECHO-G and ERA40 for a reference period. In this section we highlight the main features of the simulation performed with MM5 coupled to ECHO-G for the 1001–1990 period. We also perform some comparison with proxy-based reconstructions.

4.1 AOGCM versus RCM simulation

Figure 10 gives an overall idea of the path of the simulation. Upper panels represent the 31-yr running mean of the SAT anomalies for winter and summer with respect to the period 1900–1990. Red lines correspond to ECHO-G and blue lines to ECHO-G + MM5.

CPD
6, 2071–2116, 2010

The series are averaged over an area which covers the entire IP, including ocean grid-cells. The middle panel represent the same information but regarding the precipitation anomaly for the Northwest of the IP, meanwhile the lower panel refers to the evolution of the precipitation in the Southeast. We split the precipitation series into two areas because the precipitation regime and amount is quite different between them, as shown in Fig. 4. However SAT evolution is not so heterogeneous, so we consider just the simple average. We include ocean grid-cells to be consistent in the figure, since ECHO-G does not include any land grid-cell in the southeastern area. In this figure, the high correlation between the variations in both simulations for all seasons is apparent, and is not surprising since the AOGCM drives the RCM simulation. There are nevertheless some differences which will be commented below. In general, discrepancies in the simulations should not be seeked in the domain averaged series, but in their high resolution spatial structure, as illustrated later.

In the SAT series (upper panels of Fig. 10), we may identify a warm initial condition, followed by a cold period which roughly covers 1200–1850, and ends with a warm trend which continues until the end of the simulations. These warm/cold periods match well with respective historical periods that are relatively well documented in other parts of the world and commonly denominated as the Medieval Warm Period and the Little Ice Age. The final warming trend from roughly 1850 to the end of the simulation is simultaneous with the rise of the concentration of GHGs as prescribed in the model run (Fig. 1). The RCM tends to follow ECHO-G more weakly in summer, as we can clearly identify around 1120, 1410 or 1740 in this season.

Looking at higher frequency variability, several marked minima in the SAT anomalies can be identified around the periods 1420–1440, 1600–1620, 1675–1710 and 1810–1830, in general more noticeably in summer. Some of these cold periods match fairly well known historical periods, like the Spörer Minimum (1420–1440), the Maunder Minimum (1675–1710) and the Dalton Minimum (1810–1830), respectively. Furthermore, they seem to be directly driven by variations in the external forcing (Fig. 1). However, the model simulates a cold period around 1620 that, is not by driven by any of the

CPD
6, 2071–2116, 2010

external forcings. This aspect will be further commented in the final discussion on the context of internal variability of climate models. Interestingly, there are some minima that can be identified in all seasons, such as the Spörer minimum, whereas others, like the Maunder minimum, can hardly been identified in winter. This implies that the amplitude of the annual cycle is strongly reduced in the Maunder minimum, but not in other cold periods, and this suggests that the physical mechanism under different cold periods could be very different.

Precipitation series show in general larger differences between simulations. As in the case of SAT, this is specially noticeable in summer. The reason for this is that meanwhile winter precipitation in the IP is dominated by large scale systems (see the next section), and hence driven by the boundary conditions in the RCM, summer precipitation in the IP tends to be convective. As illustrated by Fernandez et al. (2007), the effect of the higher spatial resolution and the different physical parametrisation of both models plays an important role in this precipitation regime, and thus explains the larger differences in summer. There are also important differences between the north west and the south east of the IP, one of the most important being the large difference in the variability of the series (which is linked to the amount of precipitation). It is not so easy to identify in these series the low frequency signal of the Little Ice Age, but there exists an overall negative relationship with the SAT series, like a strong winter precipitation maximum around the Maunder Minimum and the opposite trends of both variables in summer the last century. The temporal correlation of the 31-yr running mean series of SAT and precipitation, both averaged over the whole IP, is −0.16 in winter and −0.83 in summer. Using a bootstrap method, the confidence interval for the correlation at the 95% level was found to be ±0.39 and ±0.50 for both seasons, respectively. Hence, although the winter anti correlation between precipitation and SAT can be due to chance, the summer case seems to be significant. In fact, the relationship between drier and warmer conditions in the dry season has been reported in several climate change projections for the 21th century in the Mediterranean area (Giorgi and Bi, 2005), so our findings are coherent with these results, and reinforce

CPD
6, 2071–2116, 2010

some conclusions of these studies in a past climate context. In winter this relationship is weaker due to the positive tendency of both, the precipitation and SAT.

As commented above, differences in the climatologies developed by the RCM and the AOGCM simulations are found at regional scales. For illustration, Fig. 11 depicts the summer and winter SAT anomalies in the Maunder minimum with respect to the 1900–1990 period as simulated by ECHO-G (left) and ECHO-G + MM5 (centre) and reconstructed by Luterbacher et al. (2004) (right). In this section we focus on the differences between the AOGCM and the RCM. Although it is shown in the figure, comparison with proxy-based reconstructions is performed in the next section. The spatial average of the anomalies in both simulations is similar, as can be appreciated in Fig. 10. Furthermore, anomalies are overall larger in summer than in winter in both simulations. However, the spatial distribution of the coldest areas is different. In the ECHO-G simulation they are located outside of the IP, decreasing to the southeast towards the Mediterranean Sea. The spatial structure of the anomalies is similar in both seasons. In the RCM simulation the coldest areas are rather located in the centre of the peninsula in summer, and in the higher areas in winter. It is interesting to note that similar spatial patterns, with the same seasonal cycle, were found for the warming patterns in regional climate change projections for the same area (Gómez-Navarro et al., 2010). Differences between models could be related to the coarse topography implemented in the AOGCM, as the south half part of the IP is defined as ocean, as can be seen in Fig. 2. Similar differences are apparent for the rest of seasons and for the other cold periods (not shown).

Similarly, Fig. 12 shows the same information that Fig. 11 but regarding precipitation anomalies: winter and summer anomalies in the Maunder minimum for ECHO-G, ECHO-G + MM5 and reconstructed by Pauling et al. (2006). ECHO-G simulates a homogeneous increase in precipitation about 20% for most of the IP in summer, and slightly higher in the West of the IP in winter. However, although the RCM also simulates an averaged increase of precipitation in both seasons (see Fig. 10), its shape is very different. In fact, the high resolution model simulates a strong increase in

CPD
6, 2071–2116, 2010

precipitation in some areas of the Southwest of the IP. However, there are some areas in the Southeast where there is no increase of precipitation. This behaviour is inverted in autumn for the same period, where a strong increase of precipitation is observed in the Southeast in the MM5 simulation which is not present in ECHO-G (not shown).

The differences in the shape of anomalies of SAT and precipitation in both simulations are partly due to the higher spatial resolution of the RCM, which allows it to develop a more realistic local dynamic. There is also an important contribution attributable to the more complete parametrisation of the sub-grid physical processes, which strongly modulates the simulation of precipitation. Finally, there is a component of internal variability due to the RCM itself, which may affect noticeably the evolution of the precipitation. These regional differences further illustrate how the RCM, although driven by the AOGCM, is able to develop quite different climatologies at local scales. This may impact the inter comparisons between proxy-based reconstructions and model simulations, as the AOGCMs are not able to simulate local circulations which strongly modulate observed climate in a given area.

4.2 Comparison with proxy-based reconstructions

Figure 13 shows the evolution of the anomalies in SAT (upper panel), northwest precipitation (middle panel) and southeast precipitation (lower panel) for the ECHO-G + MM5 simulation (blue line) and the corresponding reconstructions of SAT (Luterbacher et al., 2004) and precipitation (Pauling et al., 2006). As in the Fig. 10, the anomalies are calculated with respect to the period 1900–1990, but in this case ocean grid-cells of the model have not been considered to be coherent with the reconstructions. SAT winter series show similar variability in the model and the reconstruction. There is also a clear positive trend at the end of the period in both series, although in the model it begins around 50 yr earlier. In summer, reconstructions show less variability than the model, although the final trends are similar. The main difference is that, in both seasons, the model is between 0.5 and 1 K colder than the reconstructions. Overall, the agreement

CPD
6, 2071–2116, 2010

between model and reconstructions in the cold periods is not good. In the columns 2 and 3 of Fig. 11 we compare the winter and summer SAT anomalies for the Maunder minimum. The reconstruction does not present the strong cold anomaly in summer SAT simulated by both models. There is a better agreement in winter in the intensity of the coldness, although the spatial structure of the anomaly is very different.

Precipitation tends to be overestimated by the model in both season in the northwest (see series in the middle panel in Fig. 13). Variability of winter series precipitation for the model and the reconstruction is similar for both the wet and dry areas of the IP. There is also a good agreement in the upward final trend. Summer precipitation variability is nevertheless overestimated by the model in the wet area and underestimated in the dry area. Correlation between the model and the reconstruction is rather low. In columns 2 and 3 of Fig. 12 we compare the winter and summer precipitation anomalies for the Maunder minimum (1671–1700). The spatial structure of precipitation anomalies do not agree and the average value is also quite different. In particular, the reconstruction shows a strong decrease of precipitation in the south in summer that is opposite to the result obtained with the model.

We have explored the causes of the positive anomalies in precipitation in this period. The NAO is a well known variability pattern in the sea level pressure (SLP) field that affects the climate of the North Atlantic-European sector. It is usually defined for winter, when its effects are more apparent. However, its summer counterpart has also been found to influence the summer climate in this area (Folland et al., 2009). To ensure that the relationship between the NAO and the precipitation over the IP is robust in the observed climate, we have calculated the correlation between the average precipitation in the IP and SLP in the period 1950–2000. To perform these calculations we have used the ECA data base of precipitation over the IP (Haylock et al., 2008) and the NCEP reanalysis (Kalnay et al., 1996) for SLP. The correlation map for winter has a dipolar structure that is very similar to the NAO pattern defined as the leading EOF pattern of the SLP field defines the NAO (not shown). The correlation pattern shows that over the IP the (negative) correlation between SLP and precipitation is below −0.8,

CPD
6, 2071–2116, 2010

illustrating the strong influence of NAO in the winter precipitation over the IP, which has been previously pointed out by Trigo et al. (2004). The correlations pattern changes in summer, and it is similar to the summer NAO described by Folland et al. (2009) (not shown). Although the sensitivity of summer precipitation over the IP to variations of SLP is weaker than in winter, the correlation is −0.4 for the wettest areas in the northwest. Thus, the NAO variations play an important role in the precipitation of the IP.

We have investigated the link between the NAO variations and the precipitation within the models. The NAO index for each season is defined here as the standardised series of the principal component associated to the leading EOF of the mean SLP in the corresponding season in an area from 70° W to 50° E and from 20° N to 75° N. We have calculated the index using the data simulated by the AOGCM, since the former area lies outside our regional simulation. Figure 14 depicts the precipitation anomaly series for the IP domain together with the corresponding NAO index for winter and summer. In winter (upper panel) the Maunder minimum is characterised by the positive anomaly in precipitation indicated above. It can now be linked to the strong minimum in the NAO index. A similar behaviour can be found around the Dalton minimum. In fact, there is a clear anti-correlation between both series. In summer (bottom panel) this anti-correlation is less apparent, although it exists in the Maunder minimum, with its maximum precipitation (minimum summer NAO) around 1690. It is important to note that a complementary explanation for the positive anomalies in this period in the summer precipitation is the higher winter precipitation due to a weaker winter NAO, since precipitation in both seasons can be related through the larger moisture content of the soil.

Hence, according to the Fig. 14, the model reproduces the observed relationship between the NAO and the precipitation over the IP. In particular, the positive precipitation anomaly in the Maunder minimum seems to be driven by a weaker NAO phase within the model. This gives us an opportunity to test the precipitation reconstructions over the IP against independent reconstructions of the NAO index. The argument is

CPD
6, 2071–2116, 2010

as follows: we should not expect in principle a good temporal agreement between the NAO index in the model and in the reconstructions, since this circulation mode is strongly dominated by random internal variability. Nevertheless the model is complex enough to simulate realistically the physical mechanism which link the evolution of NAO and precipitation in the IP. Thus, if the NAO evolution in a given period in the model is, by chance, in phase with the evolution of the actual climate, the precipitation pattern developed by the model in that period would be a reliable version of the precipitation in the actual climate, and then it can be compared with precipitation reconstructions to check if they are consistent. Trouet et al. (2009) have performed a reconstruction of the NAO index for a 947 yr period which largely overlaps with the present simulation. Their reconstruction (shown in green in the Fig. 14) is characterised by a strong NAO phase in the Medieval Climate Anomaly (roughly from 1100 to 1400) followed by a weakening during the Little Ice Age. Between the Maunder and Dalton minima this NAO reconstruction depicts its lower value, and hence qualitatively supports the idea of a weaker NAO in the cold periods which would be responsible of an increment in the precipitation rates in the IP in this period, enforcing the results of the simulation rather than the Pauling et al. (2006) precipitation reconstruction. A possible explanation for the differences between the model and the precipitation reconstructions is the lack of a considerable number of proxies available over the IP that were used for this reconstruction.

5 Summary and conclusions

The high spatial resolution simulation described in the previous sections represents an added value to previous paleosimulation performed with ECHO-G (Zorita et al., 2005, and references herein). By means of a comparison with a dynamic downscaling performed with reanalysis data, MM5 was shown to be able to improve significantly the skill of ECHO-G when reproducing the observed climate in the IP in the 1961–1990 period. In particular, differences between climate developed in ERA40 and ECHO-G

CPD
6, 2071–2116, 2010

are larger than those for the corresponding regionalizated data sets. Thus, the RCM narrows the differences between these two simulations. Furthermore, MM5 is able also to narrow differences between the climate developed by ECHO-G and the ECA data base. This supports the idea than the regionalization of a AOGCM paleosimulation may improve the quality of this model-based reconstructions at regional scales. These improvements regard the modification of the seasonal variability, which is modified by MM5 in the sense of make it more similar to observations in the reference period. Nevertheless there are some differences in the simulations with respect to the observations in the reference period which are attributable to the inherent internal variability of the model, thus difficulting the assessing of the skill of the model.

External forcings seem to have an important role in the simulation. There is a series of minima and maxima in the TSI which drive corresponding cold/warm periods, and match with several known historical periods. In particular, the models are able to simulate the Little Ice Age and the Medieval Optimum as a direct response to radiation forcing. On the other hand, in the last 150 yr of the 20th century there is an increase of the temperature, which seems to be linked to the continuous rise of GHGs concentrations characteristic of the industrial period. There are nevertheless some cold minima that can not be explained by the external forcings, for instance in the period 1600–1620. This minimum seems to be caused by the internal characteristic variability of the AOGCM. If this is the case, this introduces an important uncertainty factor, since the amplitude of the internal variability could in principle even explain all the simulated minimum at this regional scales. This amplitude can be better estimated by an ensemble of simulations using different AOGCMs, or even using the same AOGCM with different initial conditions. This aspect will be further explored in future studies.

Although domain-averaged values of SAT and precipitation in the RCM simulation are very similar to those for the AOGCM in the same area, some important differences appear at regional scales. These can be found in the shape and intensity of SAT and precipitation anomaly patterns. Regarding precipitation, MM5 simulates an anomaly pattern which is qualitatively different to the one simulated by ECHO-G for

CPD
6, 2071–2116, 2010

the Maunder minimum. The improvement achieved by the regionalization can be attributable to the higher spatial resolution and more complete physical parametrisation of sub-grid processes. The differences introduced by the RCM may have an important impact in the inter comparison exercises between proxy-based reconstructions and model simulations.

We have compared the results of the model simulation with the SAT and precipitation reconstruction of Luterbacher et al. (2004) and Pauling et al. (2006) over the Iberian Peninsula, respectively. The model results tend to be colder than the reconstruction, more noticeably in the Little Ice Age. Winter SAT variability is similar, but in summer the reconstruction depicts less variability. There is a relatively good agreement in the final trend in the 20th century. Precipitation series show similar variability in the model and in the reconstructions, although the correlation between both is low. In particular the reconstruction does not seem to reproduce the positive anomaly in precipitation simulated by the model in the past centuries. The comparison with a recent NAO reconstruction (Trouet et al., 2009) seems to support the results of the model, and thus differences between both results could be attributable to the few quality proxies over the IP employed in the reconstruction. This disagreement between reconstructed and simulated precipitation is important because it can be carried further to place confidence in the simulations of future climate in the Iberian Peninsula and the Mediterranean region in general. Climate projections indicate a strong decrease of precipitation in this region (Giorgi and Bi, 2005) with a high level of agreement across the suite of IPCC models (IPCC, 2007). The ECHO-G model, also included in the IPCC suite, also simulates strong decreases of winter precipitation in the future under increasing concentrations of greenhouse gases. If the sign of the simulated precipitation changes disagrees with that of the reconstructions, the confidence placed on the future projections at regional scales would be compromised.

As future work, further intercomparisons between the the RCM simulation and newer proxy data reconstructions that are being developed at this moment in the IP will be performed in order to validate more aspects of the simulation. On the other hand, more

CPD
6, 2071–2116, 2010

simulations will be carried out using different AOGCM simulations. The aim of these ensemble of simulations is to evaluate the importance of the internal variability of the AOGCM driving the simulation, and trying to separate its effect from the impact of the external forcings.

Acknowledgements. This work was funded by the Spanish Ministry of the Environment (project SALVA-SINOVAS, Ref. 200800050083542) and the Spanish Ministry of Science and Technology (project SPECMORE -CGL2008-06558-C02-02/CLI). The authors also gratefully acknowledge the funding from the Euro-Mediterranean Institute of Water (IEA). J. J. Gómez-Navarro thanks the Spanish Ministry of Education for his Doctoral scholarship (AP2006-04100).

References

Ammann, C. M., Joos, F., Schimel, D. S., Otto-Bliesner, B. L., and Tomas, R. A.: Solar influence on climate during the past millennium: results from transient simulations with the NCAR Climate System Model, P. Natl. Acad. Sci. USA, 104, 3713–3718, doi:10.1073/pnas.0605064103, 2007. 2073

Bradley, R. S. and Jonest, P. D.: "Little Ice Age" summer temperature variations: their nature and relevance to recent global warming trends, Holocene, 3, 367–376, doi:10.1177/095968369300300409, 1993. 2072, 2073

Chen, F. and Dudhia, J.: Coupling an advanced land surface-hydrology model with the Penn State-NCAR MM5 modeling system – part 1: model implementation and sensitivity, Mon. Weather Rev., 129, 569–585, 2001a. 2077

Chen, F. and Dudhia, J.: Coupling an advanced land surface-hydrology model with the Penn State-NCAR MM5 modeling system – part 2: preliminary model validation, Mon. Weather Rev., 129, 587–604, 2001b. 2077

Demuzere, M., Werner, M., van Lipzig, N. P. M., and Roeckner, E.: An analysis of present and future ECHAM5 pressure fields using a classification of circulation patterns, Int. J. Climatol., 29, 1796–1810, doi:10.1002/joc.1821, 2009. 2082

Dudhia, J.: Numerical study of convection observed during the winter monsoon experiment using a mesoscale two-dimensional model, J. Atmos. Sci., 46, 3077–3107, 1989. 2077

CPD
6, 2071–2116, 2010

Dudhia, J.: A nonhydrostatic version of the Penn StateNCAR mesoscale model: validation tests and simulation of an Atlantic cyclone and cold front, Mon. Weather Rev., 121, 1493–1513, 1993. 2076

Fernández, J., Montávez, J. P. Sáenz, J. González-Rouco, J. F., and Zorita, E.: Sensitivity of the MM5 mesoscale model to physical parameterizations for regional climate studies: annual cycle, J. Geophys. Res.-Atmos., 112, D04101, doi:10.1029/2005JD006649, 2007. 2077, 2088

Folland, C. K., Knight, J., Linderholm, H. W., Fereday, D., Ineson, S., and Hurrell, J. W.: The summer North Atlantic oscillation: past, present, and future, J. Climate, 22, 1082–1103, 2009. 2091, 2092

Font-Tullot, I.: Climatología de España y Portugal, Ediciones Universidad de Salamanca, Salamanca, 2nd edition, 2000. 2076

Giorgi, F. and Bi, X.: Updated regional precipitation and temperature changes for the 21st century from ensembles of recent AOGCM simulations, Geophys. Res. Lett., 32, L21715, doi:10.1029/2005GL024288, 2005. 2088, 2095

Gómez-Navarro J. J., Montávez, J. P., Jiménez-Guerrero, P., Jerez, S., and García-Valero, J. A.: Warming patterns in regional climate change projections over the Iberian Peninsula, Meteorol. Z., 19, 275–285, 2010. 2076, 2084, 2086, 2089

González-Rouco, J. F., Beltrami, H., Zorita, E., and Stevens, M. B.: Borehole climatology: a discussion based on contributions from climate modeling, Clim. Past, 5, 97–127, doi:10.5194/cp-5-97-2009, 2009. 2073

Grell, G. A.: Prognostic evaluation of assumptions used by cumulus parameterizations, Mon. Weather Rev., 121, 764–787, 1993. 2077

Grell, G. A., Dudhia, J., and Stauffer, D. R.: A description of the fifth-generation Penn State/NCAR Mesoscale Model (MM5), Tech. Rep. NCAR/TN-398+STR, National Center for Atmospheric Research, 1994. 2076

Haylock, M. R., Hofstra, N., Tank, A. M. G. K., Klok, E. J., Jones, P. D., and New, M.: A European daily high-resolution gridded data set of surface temperature and precipitation for 1950–2006, J. Geophys. Res.-Atmos., 113, D20119, doi:10.1029/2008JD010201, 2008. 2077, 2091

Hong, S. Y. and Pan, H. L.: Nonlocal boundary layer vertical diffusion in a medium-range forecast model, Mon. Weather Rev., 124, 2322–2339, 1996. 2077

CPD
6, 2071–2116, 2010

Hostetler, S., Bartlein, P., Clark, P., Small, E., and Solomon, A.: Simulated influences of Lake Agassiz on the climate of Central North America 11 000 yr ago, Nature, 405, 334–337, 2000. 2074

Huybers, P. and Curry, W.: Links between annual, Milankovitch and continuum temperature variability, Nature, 441, 329–332, doi:10.1038/nature04745, 2006. 2073

IPCC: Climate Change 2007: The Physical Science Basis: Contribution of Working Group I to the Fourth Assessment Report of the Intergovernmental Panel on Climate Change, Cambridge University Press, New York, 2007. 2095

Jacob, D., Barring, L., Christensen, O. B., Christensen, J. H., de Castro, M., Deque, M., Giorgi, F., Hagemann, S., Lenderink, G., Rockel, B., Sanchez, E., Schaer, C., Seneviratne, S. I., Somot, S., van Ulden, A., and van denHurk, B.: An inter-comparison of regional climate models for Europe: model performance in present-day climate, Climatic Change, 81, 31–52, doi:10.1007/s10584-006-9213-4, 2007. 2074, 2077

Jerez, S. Montávez, J. P., Gómez-Navarro, J. J., Jiménez-Guerrero, P., Jiménez, J. M.: Temperature sensitivity to the land-surface model in MM5 climate simulations over the Iberian Peninsula, Meteorol. Z., 19, 1–12, 2010. 2075, 2077, 2078

Jones, P., Osborn, T., and Briffa, K.: The evolution of climate over the last millennium, Science, 292, 662–667, 2001. 2072, 2073

Jones, P. D., Briffa, K. R., Osborn, T. J., Lough, J. M., van Ommen, T. D., Vinther, B. M., Lutherbacher, J., Wahl, E. R., Zwiers, F. W., Mann, M. E., Schmidt, G. A., Ammann, C. M., Buckley, B. M., Cobb, K. M., Esper, J., Goosse, H., Graham, N., Jansen, E., Kiefer, T., Kull, C., Kuettel, M., Mosley-Thompson, E., Overpeck, J. T., Riedwyl, N., Schulz, M., Tudhope, A. W., Villalba, R., Wanner, H., Wolff, E., and Xoplaki, E.: High-resolution palaeoclimatology of the last millennium: a review of current status and future prospects, Holocene, 19, 3–49, doi:10.1177/0959683608098952, 2009. 2073

Kalnay, E., Kanamitsu, M., Kistler, R., Collins, W., Deaven, D., Gandin, L., Iredell, M., Saha, S., White, G., Woollen, J., Zhu, Y., Leetmaa, A., and Reynolds, R.: The NCEP/NCAR 40-yr reanalysis project, B. Am. Meteorol. Soc., 77, 437–470, 1996. 2091

Legutke, S. and Voss, R.: The Hamburg atmosphere-ocean coupled circulation model ECHO-G, Tech. rep., DKRZ, Hamburg, Germany, 1999. 2075

Luterbacher, J., Dietrich, D., Xoplaki, E., Grosjean, M., and Wanner, H.: European seasonal and annual temperature variability, trends, and extremes since 1500, Science, 303, 1499–1503, 2004. 2073, 2075, 2078, 2089, 2090, 2095

CPD
6, 2071–2116, 2010

Mann, M. E., Zhang, Z., Hughes, M. K., Bradley, R. S., Miller, S. K., Rutherford, S., and Ni, F.: Proxy-based reconstructions of hemispheric and global surface temperature variations over the past two millennia, P. Natl. Acad. Sci. USA, 105, 13252–13257, doi:10.1073/pnas.0805721105, 2008. 2072, 2073

Mlawer, E. J., Taubman, S. J., Brown, P. D., Iacono, M. J., and Clough, S. A.: Radiative transfer for inhomogeneous atmospheres: RRTM, a validated correlated-model for the longwave, J. Geophys. Res., 102, 16663–16682, 1997. 2077

Montávez J. P., Fernández, J., and González-Rouco, J. F.: Climate change projections over the Iberian Peninsula (in Spanish), in: V Asamblea Hispano Portuguesa de geodesia y geofísica, Ministerio de Medio Ambiente, ISBN 84-8320-373-1, Sevilla, 2006. 2076

Pauling, A., Luterbacher, J., Casty, C., and Wanner, H.: Five hundred years of gridded high-resolution precipitation reconstructions over Europe and the connection to large-scale circulation , Clim. Dynam., 26, 387–405, doi:10.1007/s00382-005-0090-8, 2006. 2075, 2078, 2089, 2090, 2093, 2095

Stevens, M., González-Rouco, J., and Beltrami, H.: North American climate of the last millennium: underground temperatures and model comparison, J. Geophys. Res.-Earth, 113, F01008, doi:10.1029/2006JF000705, 2008. 2073

Swingedouw, D., Terray, L., Cassou, C., Voldoire, A., Salas-Mélia, D., and Servonnat, J.: Natural forcing of climate during the last millennium: fingerprint of solar variability, Clim. Dynam., in press, doi:10.1007/s00382-010-0803-5, 2010. 2072, 2073

Taylor, K.: Summarizing multiple aspects of model performance in a single diagram, J. Geophys. Res.-Atmos., 106, 7183–7192, 2001. 2077

Tett, S. F. B., Betts, R., Crowley, T. J., Gregory, J., Johns, T. C., Jones, A., Osborn, T. J., Oestroem, E., Roberts, D. L., and Woodage, M. J.: The impact of natural and anthropogenic forcings on climate and hydrology since 1550, Clim. Dynam., 28, 3–34, 2007. 2073

Trigo, R., Pozo-Vazquez, D., Osborn, T., Castro-Diez, Y., Gamiz-Fortis, S., and Esteban-Parra, M.: North Atlantic oscillation influence on precipitation, river flow and water resources in the Iberian Peninsula, Int. J. Climatol., 24, 925–944, doi:10.1002/joc.1048, 2004. 2080, 2092

Trouet, V., Esper, J., Graham, N. E., Baker, A., Scourse, J. D., and Frank, D. C.: Persistent positive Norh Atlantic oscillation model dominated the Medieval Climate Anomaly, Science, 324, 78–80, doi:10.1126/science.1166349, 2009. 2093, 2095, 2116

CPD
6, 2071–2116, 2010

Uppala, S., Kallberg, P., Simmons, A., Andrae, U., Bechtold, V., Fiorino, M., Gibson, J., Haseler, J., Hernandez, A., Kelly, G., Li, X., Onogi, K., Saarinen, S., Sokka, N., Allan, R., Andersson, E., Arpe, K., Balmaseda, M., Beljaars, A., Van De Berg, L., Bidlot, J., Bormann, N., Caires, S., Chevallier, F., Dethof, A., Dragosavac, M., Fisher, M., Fuentes, M., Hagemann, S., Holm, E., Hoskins, B., Isaksen, L., Janssen, P., Jenne, R., McNally, A., Mahfouf, J., Morcrette, J., Rayner, N., Saunders, R., Simon, P., Sterl, A., Trenberth, K., Untch, A., Vasiljevic, D., Viterbo, P., and Woollen, J.: The ERA-40 re-analysis, Q. J. Roy. Meteor. Soc., 131, 2961–3012, doi:10.1256/qj.04.176, 2005. 2075, 2079

von Storch, H. and Zwiers, F.: Statistical Analysis in Climate Research, Cambridge University Press, 2007. 2078

Yoshimore, E. M., Stocker, T. F., Raible, C., and Renold, M.: Externally forced and internal variability in ensemble climate simulations of the Maunder Minimum, J. Climate, 18, 4253–4270, 2005. 2074

Zorita, E., González-Rouco, J., von Storch, H., Montávez, J., and Valero, F.: Natural and anthropogenic modes of surface temperature variations in the last thousand years, Geophys. Res. Lett., 32, 755–762, 2005. 2072, 2073, 2076, 2093

Zorita, E., Moberg, A., Leijonhufvud, L., Wilson, R. R. B., Dobrovolny, P., Luterbacher, J., Böhm, R., Pfister, C., Glaser, R., Söderberg, J., and Gonzalez-Rouco, F.: European temperature records of the past five centuries based on documentary information compared to climate simulations, Climatic Change, 101, 143–168, 2010. 2074

CPD
6, 2071–2116, 2010

Table 1. Percentage of variance explained by each EOF of the seasonal mean series of SAT.

	EOF1		EOF2		EOF3	
	ECHO-G + MM5	ERA40 + MM5	ECHO-G + MM5	ERA40 + MM5	ECHO-G + MM5	ERA40 + MM5
MAM	82.06	76.18	7.97	11.63	4.79	5.98
JJA	79.68	79.73	10.12	9.86	4.65	5.29
SON	82.95	80.14	7.67	10.88	3.28	3.29
DJF	79.21	88.56	7.32	6.91	3.28	3.29

CPD
6, 2071–2116, 2010

Table 2. Percentage of variance explained by each EOF of the seasonal mean series of precipitation.

	EOF1		EOF2		EOF3	
	ECHO-G + MM5	ERA40 + MM5	ECHO-G + MM5	ERA40 + MM5	ECHO-G + MM5	ERA40 + MM5
MAM	45.70	40.27	18.16	19.84	10.67	9.99
JJA	34.61	36.87	16.91	15.92	7.68	11.27
SON	49.82	39.50	13.04	13.42	6.05	13.30
DJF	74.07	69.65	8.29	11.04	5.25	5.21

CPD
6, 2071–2116, 2010

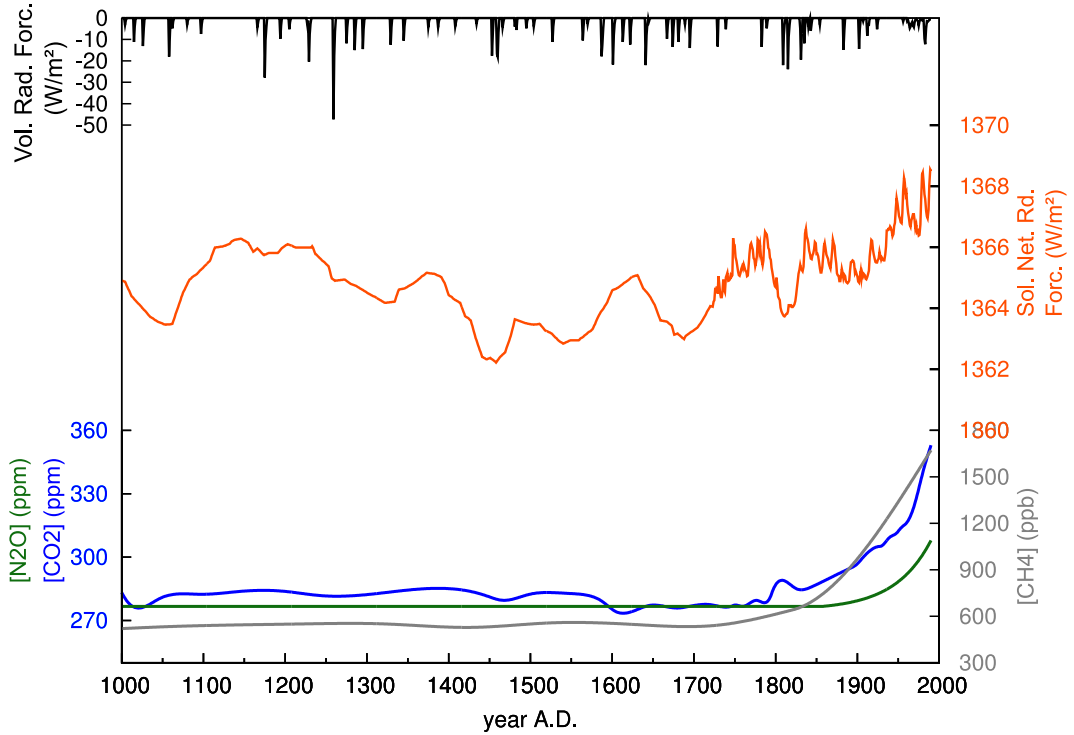

Fig. 1. Reconstruction of the forcings for the last millennium employed in the simulations. Orange line is the reconstruction of the total solar irradiance. Black line shows the estimated reduction in the effective short wave radiative balance in the top of the atmosphere due to big volcano events. Blue, green and grey lines show the evolution in the concentration of CO_2, NO_2 and CH_4, respectively.

CPD
6, 2071–2116, 2010

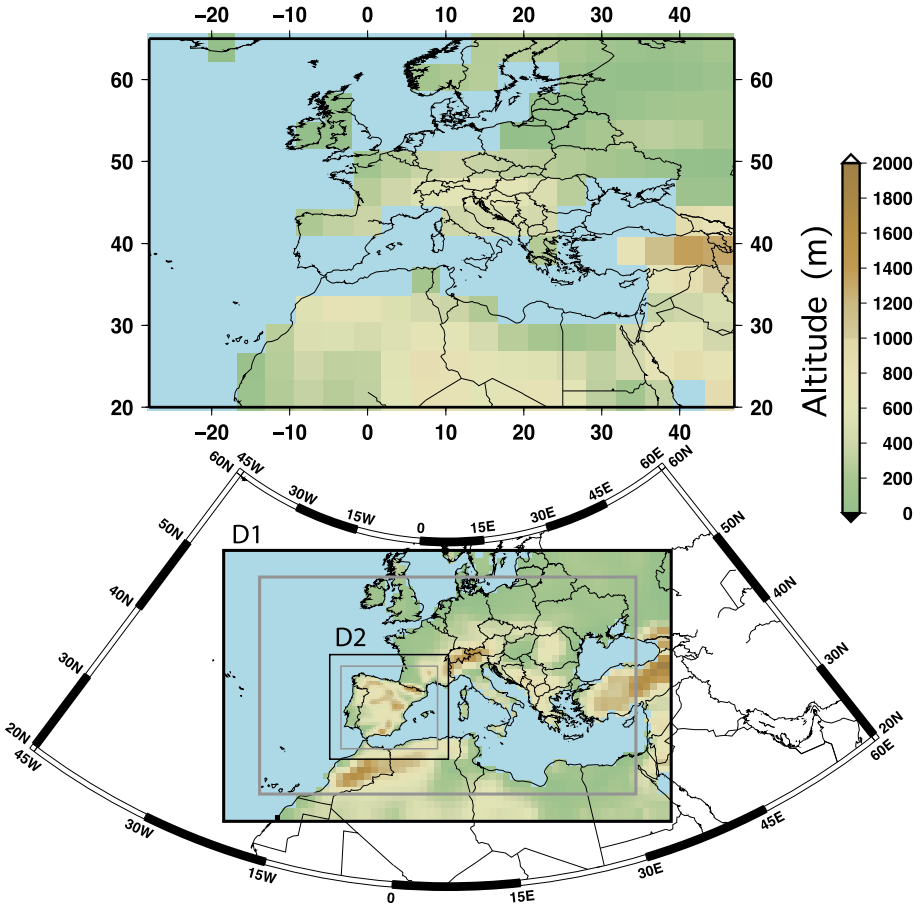

Fig. 2. Land-sea mask and orography of the AOGCM simulation (up) and spatial configuration of the two 2-way nested domains of 90 and 30 km respectively used in the RCM simulation (down). The colour of the squares in both figures represent the topography implemented in the models. Only the area inside the grey square in the domain 2 is analysed hereafter.

CPD
6, 2071–2116, 2010

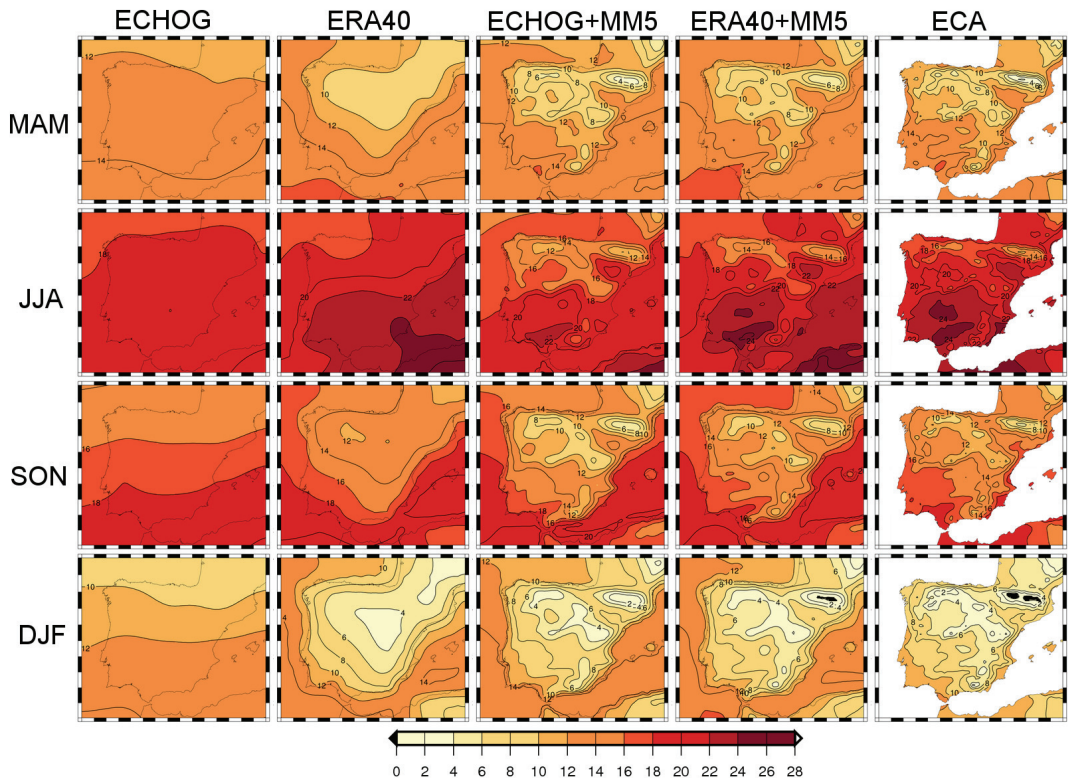

Fig. 3. Mean value of SAT (in °C) in the period 1961–1990 for ECHO-G, ERA40, and MM5 nested to both (by columns) in all the seasons (by rows). All fields have been interpolated to a 7 min regular grid to ease the visual comparison.

CPD
6, 2071–2116, 2010

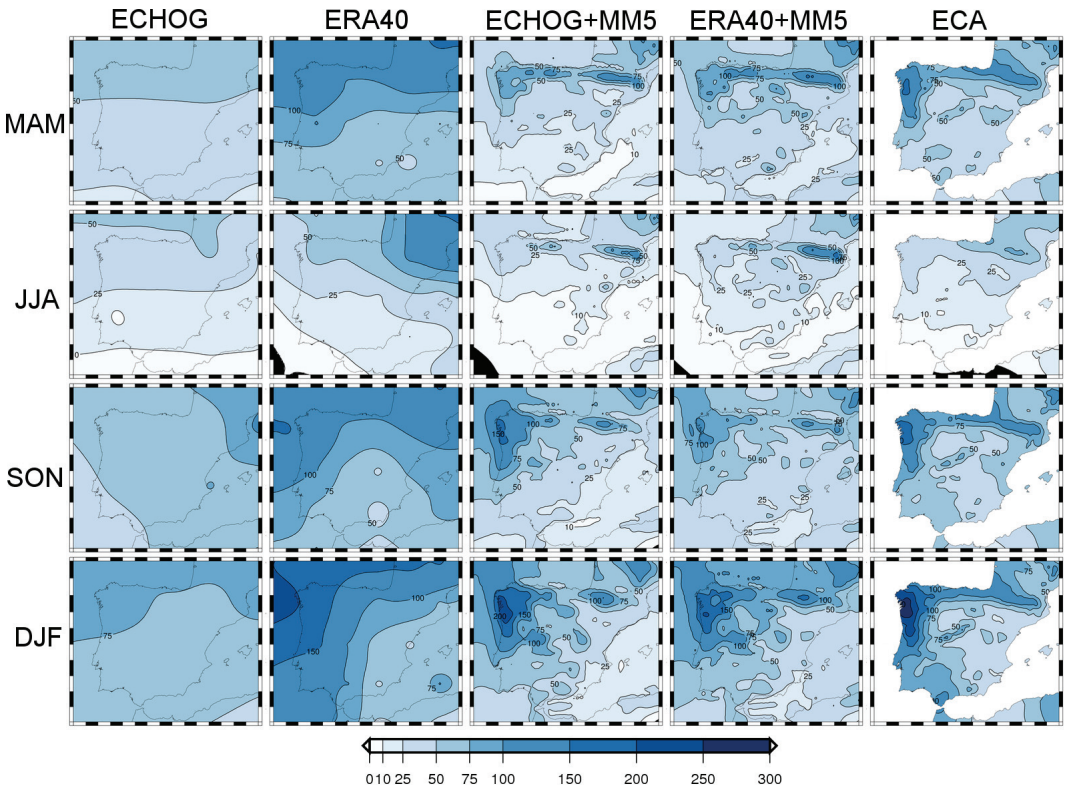

Fig. 4. Mean value of monthly precipitation (in mm/month) in the period 1961–1990 for ECHO-G, ERA40, and MM5 nested to both (by columns) in all the seasons (by rows). All fields have been interpolated to a 7 min regular grid to ease the visual comparison.

CPD
6, 2071–2116, 2010

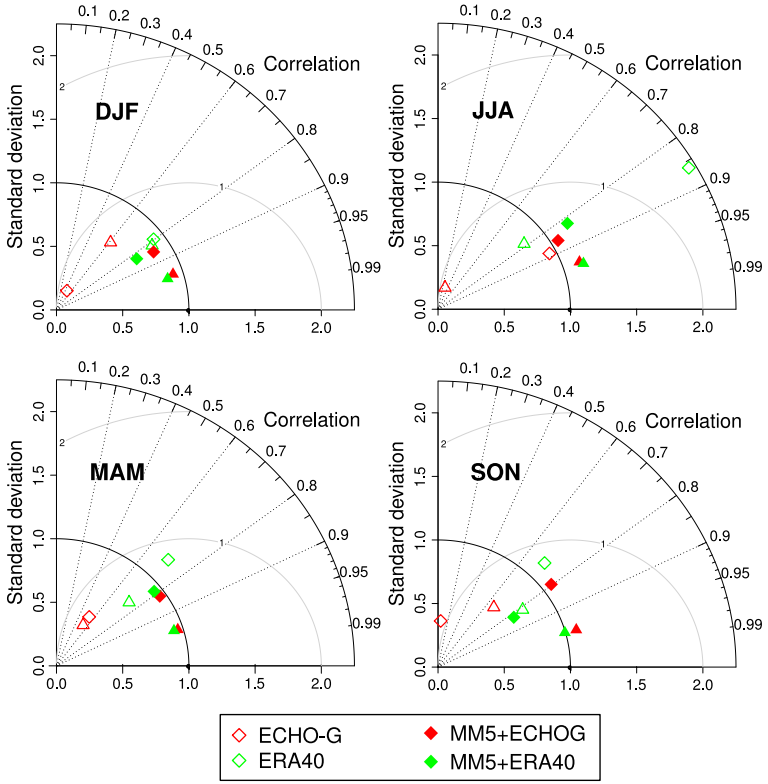

Fig. 5. Taylor diagrams of the spatial structure of the mean SAT and precipitation in the reference period. Triangles represent the correlation and variance ratio between the SAT seasonal mean values obtained by the models against the values of the ECA database. Diamonds depict the same information regarding precipitation. Empty symbols represent the driving data, meanwhile filled ones represent the MM5 results. The colour distinguishes between ECHO-G (red) and ERA40 (green). All experiments have been interpolated to the ECA grid to perform the calculations.

CPD
6, 2071–2116, 2010

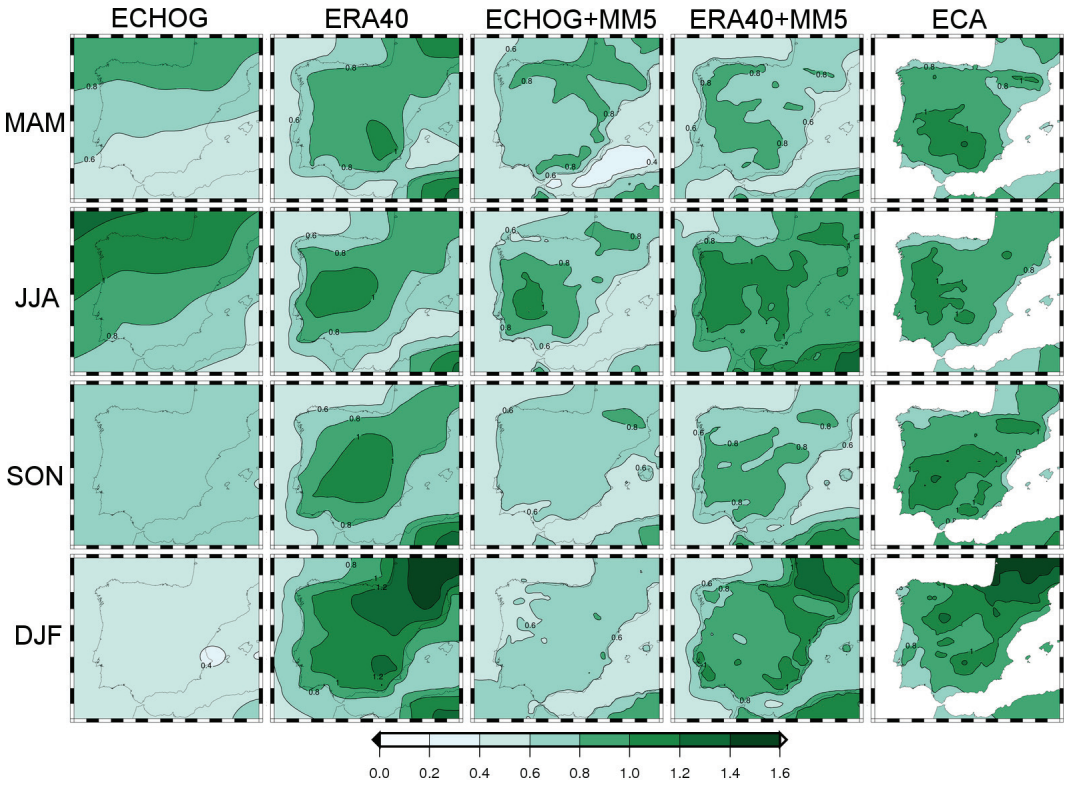

Fig. 6. Standard deviation of seasonal mean series of SAT in the period 1961–1990 for ECHO-G, ERA40, and MM5 nested to both (by columns) in all the seasons (by rows). All fields have been interpolated to a 7 min regular grid to ease the visual comparison.

CPD
6, 2071–2116, 2010

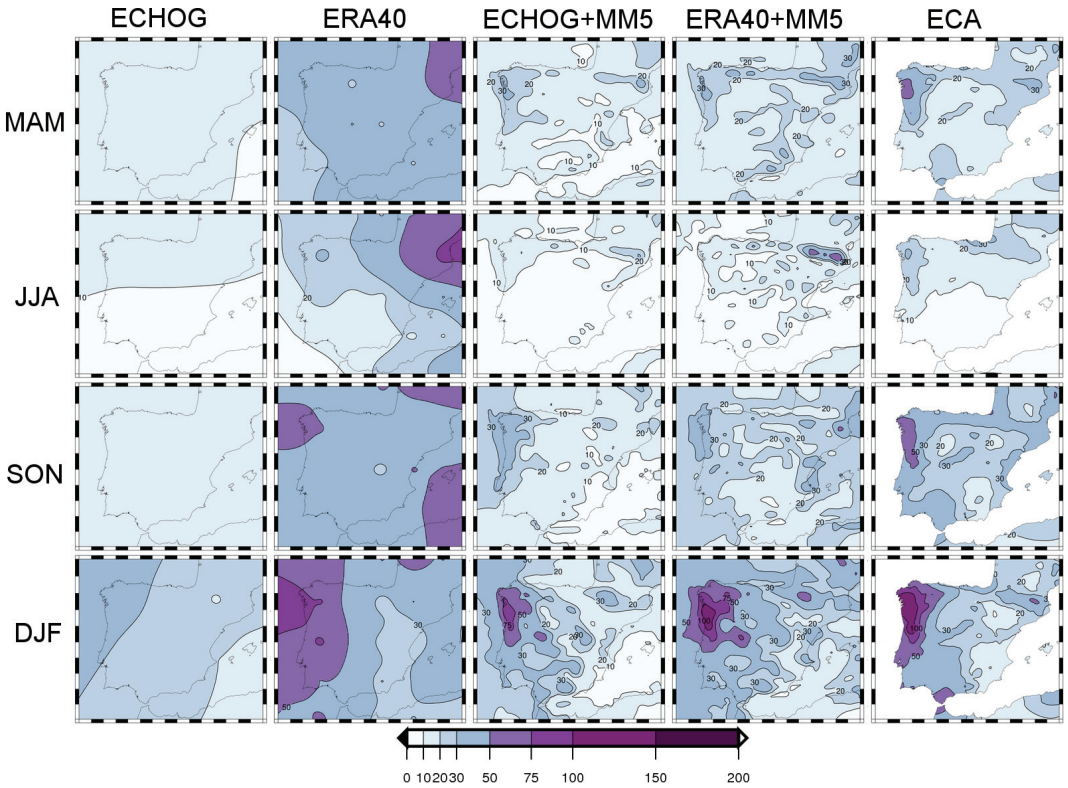

Fig. 7. Standard deviation of seasonal mean series of precipitation in the period 1961–1990 for ECHO-G, ERA40, and MM5 nested to both (by columns) in all the seasons (by rows). All fields have been interpolated to a 7 min regular grid to ease the visual comparison.

CPD
6, 2071–2116, 2010

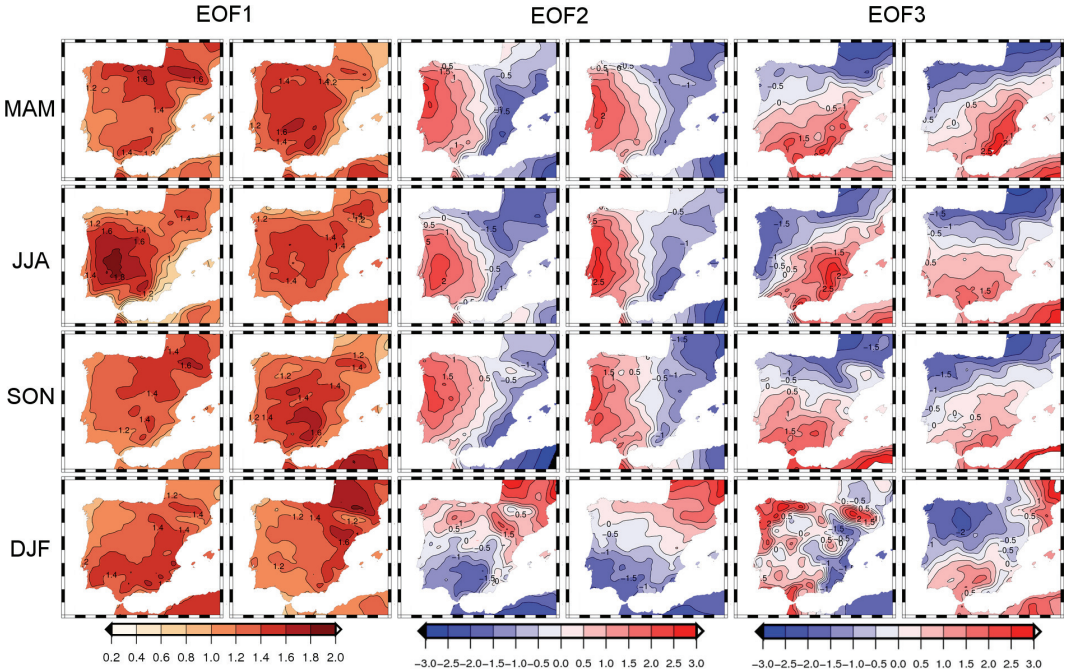

Fig. 8. Normalised EOF patterns obtained from the seasonal mean series of SAT for the period 1961–1990 in the simulations ECHO-G + MM5 and ERA40 + MM5.

CPD
6, 2071–2116, 2010

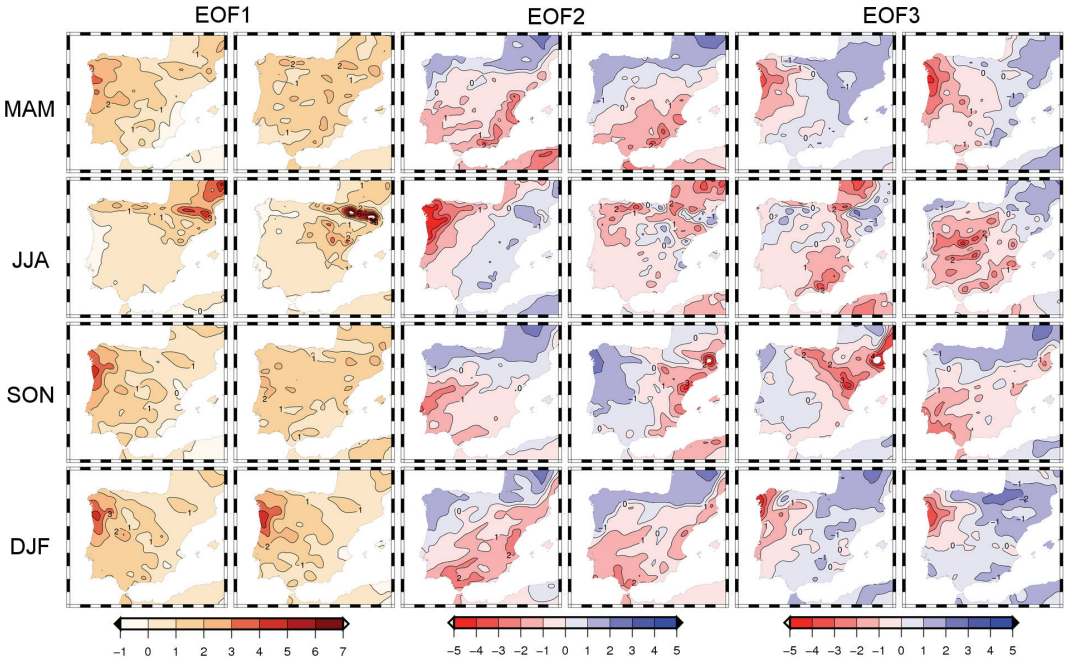

Fig. 9. Normalised EOF patterns obtained from the seasonal mean series of precipitation for the period 1961–1990 in the simulations ECHO-G + MM5 (left) and ERA40 + MM5 (right).

CPD
6, 2071–2116, 2010

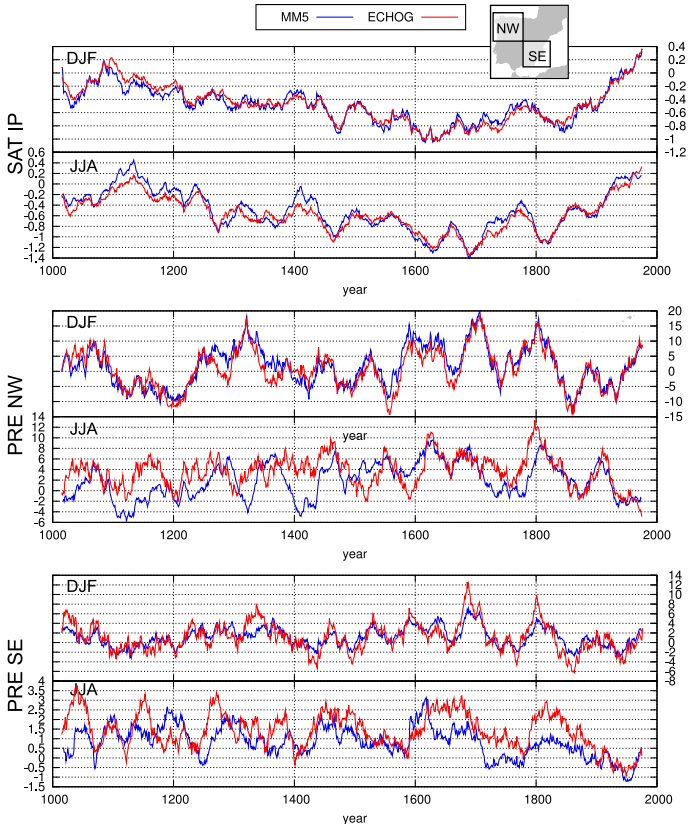

Fig. 10. Anomaly series of SAT over the IP (upper panel, in Kelvin) northwest precipitation (middle panel, in mm/month) and southeast precipitation (lower panel, in mm/month) in winter (DJF) and summer (JJA), respectively. Red line represents the series for ECHO-G and blue line for ECHO-G + MM5. Ocean grid-cells are also included in the calculations. Anomalies are calculated with respect to the period 1900–1990, and a 31-yr running mean have been applied to all series.

CPD
6, 2071–2116, 2010

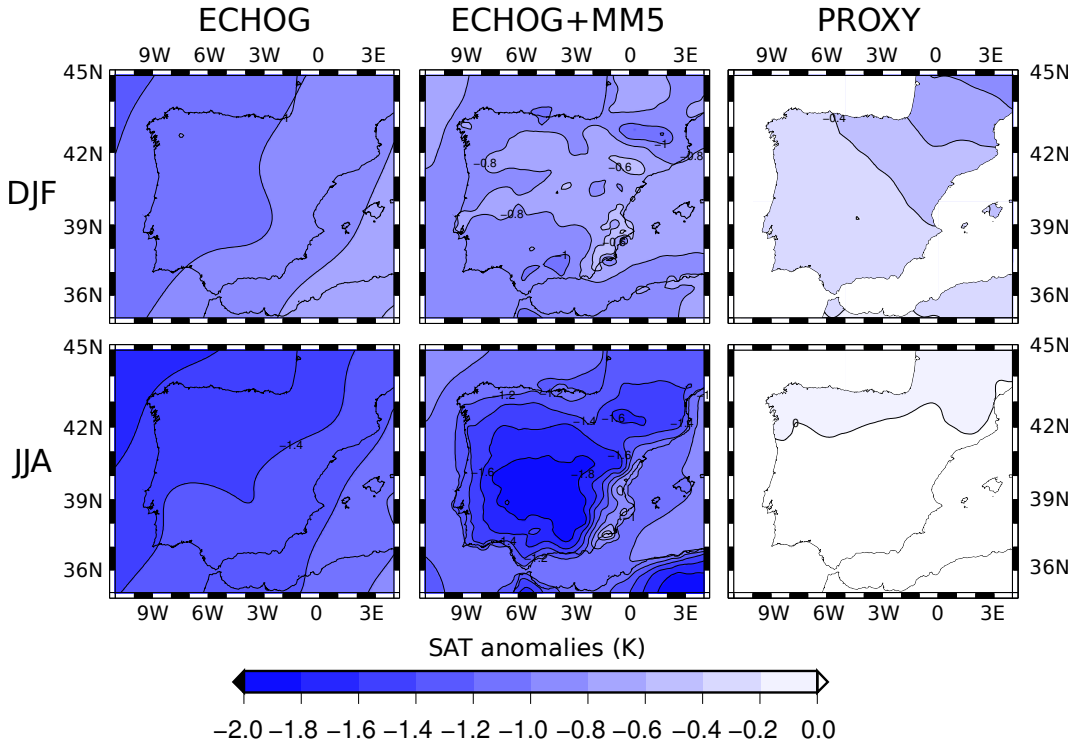

Fig. 11. SAT temperature anomalies for winter (up row) and summer (bottom row) in the 1671–1700 period respect to 1900–1990. The figure shows the results for ECHO-G (left), ECHO-G + MM5 (centre) and the SAT reconstruction (right).

CPD
6, 2071–2116, 2010

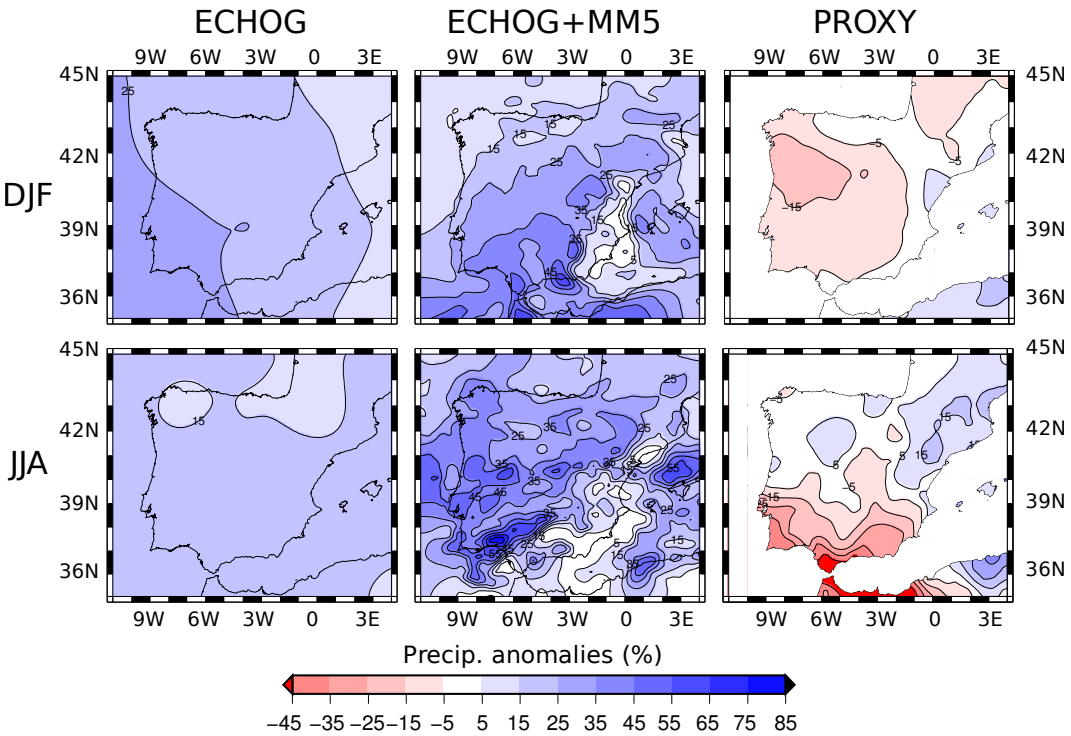

Fig. 12. Precipitation anomalies for winter (up row) and summer (bottom row) in the 1671–1700 period respect to 1900–1990. The figure shows the results for ECHO-G (left), ECHO-G + MM5 (centre) and the precipitation reconstruction (right).

CPD
6, 2071–2116, 2010

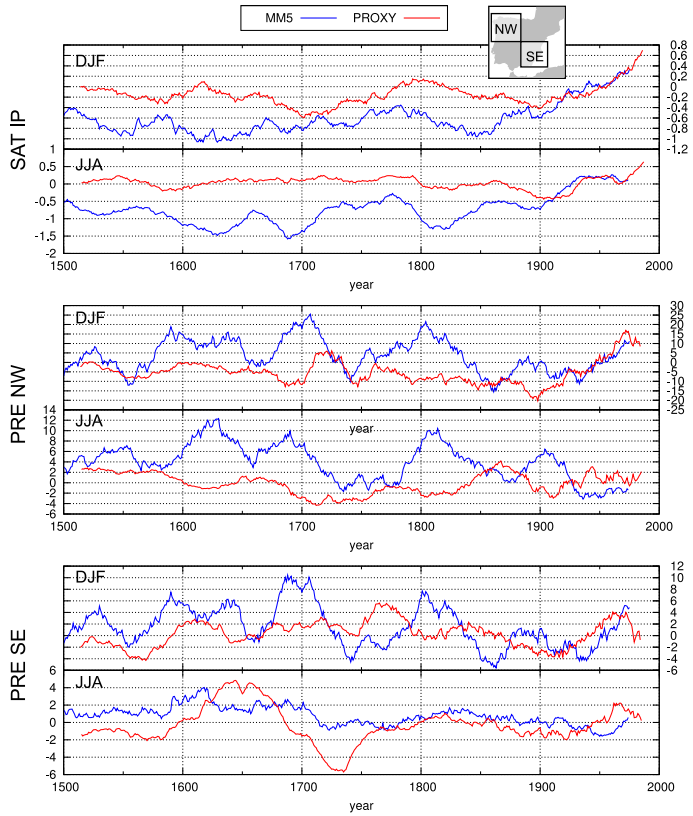

Fig. 13. Anomaly series of SAT over the IP (upper panel) northwest precipitation (middle panel) and southeast precipitation (lower panel) in winter (DJF) and summer (JJA), respectively. Red line represents the series for the reconstructions and blue line for ECHO-G + MM5. Ocean grid-cells are excluded in the calculations. Anomalies are calculated with respect to the 1900–1990 period, and a 31-yr running mean have been applied to all series.

CPD
6, 2071–2116, 2010

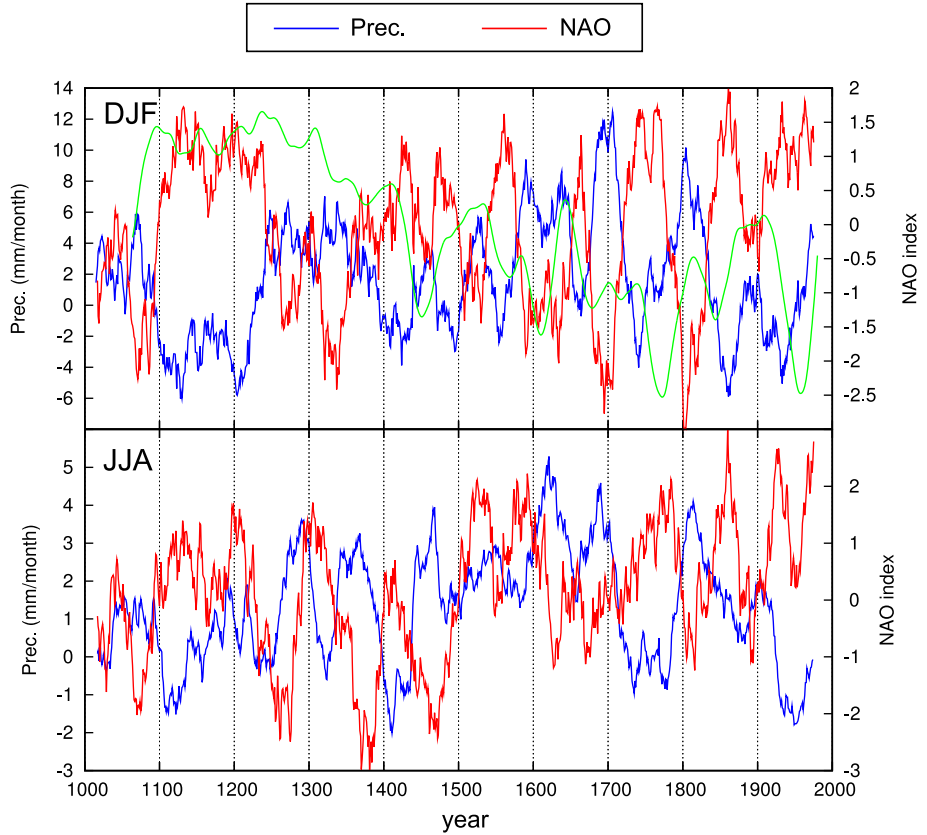

Fig. 14. Anomaly series of precipitation over the IP (blue) and NAO index (red) simulated by the model in winter (up) and summer (down). All anomalies are calculated respect to the period 1900–1990. The NAO index of the model is defined as the principal component associated to the leading EOF of the SLP in the North Atlantic-European sector (70° W to 50° E and 20° N to 75° N). Green line represents the winter NAO index reconstructed by Trouet et al. (2009).

CPD
6, 2071–2116, 2010